Dynamics of a chiral swimmer sedimenting on a flat plate

Federico Fadda [ORCID], John Jairo Molina, and Ryoichi Yamamoto [ORCID][*]

Department of Chemical Engineering, Kyoto University, Kyoto 615-8510, Japan

Three-dimensional simulations with fully resolved hydrodynamics are performed to study the dynamics of a single squirmer with and without gravity to clarify its motion in the vicinity of a flat plate. In the absence of gravity and chirality, the usual dynamics of a squirmer near a wall are recovered. The introduction of chirality modifies the swimming motion of squirmers, adding a component of motion in the third direction. When sedimentation is considered, different dynamics emerge for different gravity strength regimes. In a moderate gravity regime, neutral squirmers and pullers eventually stop moving and reorient in a direction perpendicular to the plate; by contrast, pushers exhibit continuous motion in a tilted direction. In the strong gravity regime, all squirmers sediment and reorient perpendicular to the plate. In this study, chirality is introduced to model realistic microswimmers, and its crucial effects on the nature of squirmer trajectories, which change from straight to circular, are discussed.

I. INTRODUCTION

The motion of swimming microorganisms, such as algae and bacteria, is characterized by three basic features: (1) they swim at low Reynolds numbers, where viscous forces dominate inertial ones, (2) the net force and torque exerted on the swimmers is zero, and (3) the presence of boundaries can significantly affect their swimming behavior. In nature, microorganisms regularly encounter surfaces, such as sperm swimming in the mammalian tract or bacteria forming biofilms on surfaces for spreading. Many studies related to this problem have been published [1–6].

A striking example can be seen in the accumulation of sperm on glass surfaces, reported by Rothschild [3], or in the clockwise (CW) motion that an *Escherichia coli* bacterium performs near a solid no-slip boundary, which becomes counterclockwise (CCW) near a free surface [7–11]. The physical mechanisms behind these behaviors are likely to be found in the chiral nature of the bacterium. Viewed from behind, the left-handed helical bundle of the flagella rotates in a CCW fashion, with the cell body experiencing a corresponding CW rotation. Near a no-slip surface, this CW rotation of the cell body gives rise to high viscous stresses in the gap between surfaces, which results in a translation of the cell body to the right (with respect to the axis of the body), while the flagellar bundle rotating in the reverse direction moves in the opposite direction [10], hence the CW rotation. Furthermore, in the presence of free-slip surfaces, the viscous stress between surfaces is lower, resulting in CCW trajectories. Hu *et al.* modeled the motion of *E. coli* including this chiral feature and found good agreement between the numerical simulations and experiments [12]. In recent years, the chirality has also been experimentally and theoretically investigated in the motion of cholesteric liquid crystal droplets [13–15],

active fluids [16,17], and artificial circle swimmers [18,19]. Another interesting behavior is that shown by the *Thiovulum majus* bacterium, which usually swims in helical trajectories, but when placed near surfaces, it becomes dynamically bound. In this state, cells remain free to move laterally, while their flagella point away from the surface [20]. Further examples of nontrivial motion near boundaries are seen in the case of a spherical algae called *Volvox*: when two algae swim near a solid plate, they attract each other and form bound states, in which they collectively move in a manner reminiscent of a dancing waltz or minuet [21]. Experimental observations of the scattering motion of *Chlamydomonas reinhardtii* near a plate have also been reported [22].

Swimmers in nature are also exposed to external forces that significantly affect their motions. The gravitational force is responsible for various phenomena, including bound swimmer states [21], an increase in the polar order of sedimenting swimmers [23], gravitaxis [24], inverted sedimentation [25], the rafting of active emulsion droplets [26], and the formation of phytoplankton layers in coastal oceans [27,28].

In this paper, we aim to numerically investigate the dynamics of swimming and sedimenting chiral microorganisms. To achieve this goal, we used the well-established squirmer model, introducing the rotlet dipole to incorporate the chiral nature of swimmers mentioned above [29–34]. We show that, depending on the type of squirmer involved, the magnitude of the chirality, and the gravity regime, different behaviors can be observed. In particular, the chirality is responsible for the deviation of swimmer trajectories from a straight line.

II. SIMULATION METHODS

A. The squirmer model

To model self-propelled swimmers, the squirmer model is adopted [29,30]. It consists of a spherical object with modified stick boundary conditions, with an imposed slip velocity $\boldsymbol{u}^s(\hat{\boldsymbol{r}})$

―――――
*ryoichi@cheme.kyoto-u.ac.jp

(a)

$B_1 \sin\theta\hat{\boldsymbol{\theta}}$ $B_2 \sin 2\theta\hat{\boldsymbol{\theta}}$ $C_2 \sin 2\theta\hat{\boldsymbol{\phi}}$

$B_1 > 0; B_2 < 0; C_2 > 0$

(b)
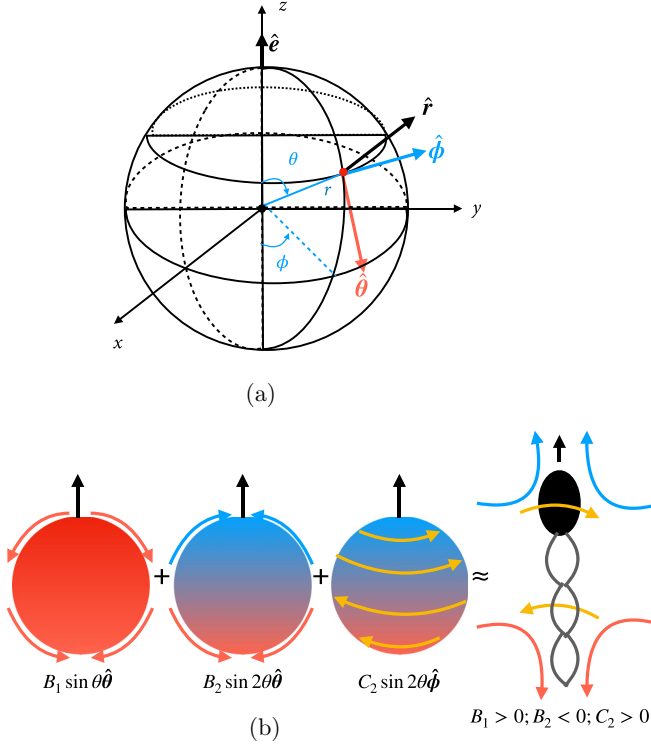
FIG. 1. (a) Definition of the unit vectors in the spherical coordinate system: $\hat{\boldsymbol{r}}$, $\hat{\boldsymbol{\theta}}$, and $\hat{\boldsymbol{\phi}}$, with $\hat{\boldsymbol{e}}$ being the swimming direction. (b) Schematic representations of the source dipole ($B_1 \sin\theta\hat{\boldsymbol{\theta}}$), stresslet ($B_2 \sin 2\theta\hat{\boldsymbol{\theta}}$), and rotlet dipole ($C_2 \sin 2\theta\hat{\boldsymbol{\phi}}$), combined to represent chiral microorganisms such as the bacterium on the right.

at its surface, which is responsible for the self-propulsion. The most general form is given as an infinite expansion of the radial, polar, and azimuthal velocity components, but for simplicity, the radial term is generally neglected [35,36]:

$$
\boldsymbol{u}^s(\hat{\boldsymbol{r}}) = \sum_{n=1}^{\infty} \frac{2}{n(n+1)} B_n P_n'(\cos\theta) \sin\theta\,\hat{\boldsymbol{\theta}}
$$
$$
+ \sum_{n=1}^{\infty} C_n P_n'(\cos\theta) \sin\theta\,\hat{\boldsymbol{\phi}}, \tag{1}
$$

where $\hat{\boldsymbol{\theta}}$, $\hat{\boldsymbol{\phi}}$, and $\hat{\boldsymbol{r}}$ are the polar, azimuthal, and radial unit vectors for a given point at the surface of the particle, $\theta = \cos^{-1}(\hat{\boldsymbol{r}} \cdot \hat{\boldsymbol{e}})$ is the polar angle and ϕ is the azimuthal angle, with $\hat{\boldsymbol{e}}$ being the swimming direction, as shown in Fig. 1(a). Usually this series expansion is truncated to the second order in the polar component, and the azimuthal terms are ignored. Here we explicitly take into account the azimuthal component (to the second order), which leads to the following slip velocity:

$$
\boldsymbol{u}^s(\theta, \phi) = B_1\left(\sin\theta + \frac{\beta}{2}\sin 2\theta\right)\hat{\boldsymbol{\theta}} + \frac{3}{2}C_2 \sin 2\theta\,\hat{\boldsymbol{\phi}}. \tag{2}
$$

The coefficient B_1 in Eq. (2) is physically related to the steady-state swimming velocity of the squirmer $v_0 = 2/3B_1$, and the ratio $\beta = B_2/B_1$ determines the pusher-puller type and its strength. When β is negative, the squirmers are pushers and generate extensile flow fields along the swimming axis;

when β is positive, the squirmers are pullers generating contractile flow fields. The case of $\beta = 0$ corresponds to a neutral squirmer. The main difference in the types of swimmers can be related to the position of the propulsion mechanism along the body. A pusher is a swimmer in which the propulsion is generated at the back (e.g., bacteria such as *E. coli*), whereas for pullers, the propulsion is located at the front (e.g., algae-like *C. reinhardtii*). In neutral swimmers (such as *Volvox*), the coefficient B_2 is small compared to B_1, which is reflected in the symmetric flow field without vorticity. Finally, the velocity field decays as r^{-3} for neutral swimmers, while it decays as r^{-2} for pushers and pullers. Regarding the azimuthal component of the surface velocity, the first term C_1 is the so-called rotlet, decaying as r^{-2}, which is neglected because it cannot exist in a torque-free system [37]. The first nontrivial coefficient C_2 is the so-called rotlet dipole, which decays as r^{-3} and is physically related to the chiral nature of swimming microorganisms, such as the previously mentioned *E. coli* [7–11,31–34,36].

To quantify the strength of the rotlet dipole, we define the chiral dimensionless parameter $\chi = C_2/B_1$. In the limiting case of $\chi = 0$, the standard squirmer model with a sticky polar surface velocity, adopted in previous works, is recovered. Figure 1(b) shows a sketch of all the polar (source dipole and stresslet) and azimuthal (rotlet dipole) components used in this study to model chiral microorganisms.

B. The smoothed profile method

To correctly solve the dynamics of the system, the coupled equations of motion for the viscous host fluid and the squirmer need to be considered [38–40]. The squirmer model is incorporated in the *smoothed profile method* (SPM), a numerical technique used to solve for the particle-fluid coupling with fully resolved hydrodynamics [41–43]. The dynamics of the particle is governed by the Newton-Euler equations of motion:

$$
\begin{aligned}
\dot{\boldsymbol{R}}_i &= \boldsymbol{V}_i, \\
\dot{\boldsymbol{Q}}_i &= \text{skew}(\boldsymbol{\Omega}_i) \cdot \boldsymbol{Q}_i, \\
M_p \dot{\boldsymbol{V}}_i &= \boldsymbol{F}_i^H + \boldsymbol{F}_i^C + \boldsymbol{F}_i^{\text{ext}}, \\
\boldsymbol{I}_p \cdot \dot{\boldsymbol{\Omega}}_i &= \boldsymbol{N}_i^H + \boldsymbol{N}_i^{\text{ext}},
\end{aligned} \tag{3}
$$

where i is the particle index, $\boldsymbol{R}_i$ and $\boldsymbol{V}_i$ are the center of mass position and velocity, respectively, $\boldsymbol{Q}_i$ is the orientation matrix, and skew ($\boldsymbol{\Omega}_i$) is the skew symmetric matrix of the angular velocity $\boldsymbol{\Omega}_i$, defined as

$$
\text{skew}(\boldsymbol{\Omega}_i) = \begin{pmatrix} 0 & -\Omega_i^z & \Omega_i^y \\ \Omega_i^z & 0 & -\Omega_i^x \\ -\Omega_i^y & \Omega_i^x & 0 \end{pmatrix}. \tag{4}
$$

The equation for $\dot{\boldsymbol{Q}}$ uses this skew-symmetric matrix to express the time evolution of the body-frame axis vectors $\hat{\boldsymbol{e}}_i^{(\alpha)}$ in matrix form ($\alpha = 1, 2, 3$), with the αth column of $\boldsymbol{Q}_i$ corresponding to $\hat{\boldsymbol{e}}_i^{(\alpha)}$. This is equivalent to the standard representation in terms of cross-products, $d/dt\,\hat{\boldsymbol{e}}_i^{(\alpha)} = \boldsymbol{\Omega}_i \times \hat{\boldsymbol{e}}_i^{(\alpha)}$, since $\boldsymbol{a} \times \boldsymbol{b} \equiv \text{skew}(\boldsymbol{a}) \cdot \boldsymbol{b}$. $\boldsymbol{I}_p (= 2/5M_p R^2 \boldsymbol{I})$ is the inertia tensor (with $\boldsymbol{I}$ being the unit tensor), and $M_p (= \frac{4}{3}\pi R^3 \rho_p)$ is the mass of a spherical particle with density ρ_p and radius R. $\boldsymbol{F}_i^H$ ($\boldsymbol{N}_i^H$) is the hydrodynamic force (torque), $\boldsymbol{F}_i^C$ is the

particle-particle force due to the steric repulsion, modeled with a Weeks-Chandler-Anderson potential with 36:18 powers, and $\boldsymbol{F}_i^{\text{ext}}$ ($\boldsymbol{N}_i^{\text{ext}}$) is the external force (torque). In this study, a gravitational force $\boldsymbol{F}_i^{\text{ext}} = -\frac{4}{3}\pi R^3 (\rho_p - \rho_f) g \boldsymbol{z}$ is applied along the vertical z axis, with g being the acceleration due to gravity and ρ_f being the density of the fluid [44–48]. The center of mass of the particle is assumed to coincide with its geometric center; however, more general cases in which they are displaced (i.e., bottom-heaviness) will result in an additional torque [49–55].

The evolution of the host fluid is governed by the Navier-Stokes equation with the incompressible condition:

$$\nabla \cdot \boldsymbol{u}_f = 0, \tag{5}$$

$$\rho_f (\partial_t + \boldsymbol{u}_f \cdot \nabla) \boldsymbol{u}_f = \nabla \cdot \boldsymbol{\sigma}_f, \tag{6}$$

$$\boldsymbol{\sigma}_f = -p\boldsymbol{I} + \eta_f [\nabla \boldsymbol{u}_f + (\nabla \boldsymbol{u}_f)^T], \tag{7}$$

where $\boldsymbol{u}_f$ is the fluid mass density, η_f is the shear viscosity, and $\boldsymbol{\sigma}_f$ is the Newtonian stress tensor. The key element of the SPM, used to solve Eqs. (3)–(6), is to replace the sharp boundaries between the solid particles and the host fluid with interfacial regions with a finite width ξ_p. For this, we introduce a smooth continuous function ϕ_p taking a value of 1 in the solid domain and 0 in the fluid domain. In this way, it is possible to define the total velocity $\boldsymbol{u}$ as

$$\boldsymbol{u} = (1 - \phi_p)\boldsymbol{u}_f + \phi_p \boldsymbol{u}_p + \phi_W \boldsymbol{u}_W, \tag{8}$$

where $(1 - \phi_p)\boldsymbol{u}_f$ is the contribution from the fluid,

$$\phi_p \boldsymbol{u}_p = \sum_i \phi_{i,p}(\boldsymbol{V}_i + \boldsymbol{\Omega}_i \times \boldsymbol{R}_i) \tag{9}$$

is the contributions from the rigid particles, and $\phi_W \boldsymbol{u}_W$ arises from the stationary flat plates placed at the top and bottom of the system, normal to the vertical z direction. In implementing the rigid flat plates, we introduce an additional phase field function ϕ_W that connects the value of 1 in the plate domain with the value of 0 outside, with a finite width ξ_W. The plate velocity is defined as $\boldsymbol{u}_W = 0$. The time evolution of the total flow field $\boldsymbol{u}$ then obeys

$$\nabla \cdot \boldsymbol{u} = 0, \tag{10}$$

$$\rho_f (\partial_t + \boldsymbol{u} \cdot \nabla)\boldsymbol{u} = \nabla \cdot \boldsymbol{\sigma}_f + \rho_f (\phi_p \boldsymbol{f}_p + \boldsymbol{f}_{sq}). \tag{11}$$

Here $\phi_p \boldsymbol{f}_p$ and $\boldsymbol{f}_{sq}$ are two constraint forces, with the former needed to maintain the rigidity of the particles and the latter needed to maintain the squirming velocity at the particle-fluid interface. Within the SPM, we solve the coupled Navier-Stokes and rigid-body equations of motion using a staggered-step procedure. First, assuming a one-component fluid representation, we solve for the advection and diffusion contributions to the Navier-Stokes equation and update the particle positions and orientations. Then the change in momentum within the particle domain is computed and used to calculate the hydrodynamic forces and torques on the particles. Requiring momentum conservation between the fluid and particle domains provides the relationship between $\phi \boldsymbol{f}_p$ and either $\boldsymbol{F}^H$ or $\boldsymbol{N}^H$, allowing us to update the particle velocities in a self-consistent manner. Finally, the updated particle velocities

are used to compute the squirming boundary conditions and thus $\boldsymbol{f}_{sq}$. A detailed description of the SPM algorithm can be found in Refs. [41–43].

III. RESULTS

A. Swimming near a wall

In this first situation, we analyzed the dynamics of a squirmer swimming near a flat wall in the absence of gravity. This case corresponds to $\boldsymbol{F}_i^{\text{ext}} = 0$ and $\rho_p/\rho_f = 1$. We considered Re $= \rho_f v_0 2R/\eta_f = 0.1$. This choice was made mainly for numerical convenience to keep the simulation times within a reasonable limit while staying within a regime where inertial effects are negligible [1–6]. The radius and the interface width of the particle and wall were set to $R = 5\Delta$, $\xi_p = 2\Delta$ and $\xi_W = 4\Delta$, respectively, where $\Delta = 1$ is the grid spacing. The shear viscosity η_f and the fluid density ρ_f were set to 1. The system was a cubic simulation box of lateral size $L = 64\Delta$. For these simulations, we placed a single squirmer at an initial position $(L/2\Delta, L/2\Delta, L/7\Delta)$ near the bottom plate, with its swimming axis along the y direction, tilted towards the plate with an initial angle $\delta_0 = 135°$. The case of $0° \leqslant \delta_0 \leqslant 90°$, with a squirmer initially perpendicular or parallel to the plate [as indicated in Fig. 2(a)], is not interesting, as the squirmer always swims away from the surface. However, if the squirmer swims towards the wall, a rich variety of dynamical modes can be observed. We also checked to ensure that our results do not qualitatively change upon variation of the value of the initial tilt angle. We performed a set of simulations in the range of parameter values $\beta \in [-5, 5]$ and $\chi \in [-5, 5]$.

Figure 2(b) shows the swimming heights of different nonchiral ($\chi = 0$) squirmers, measured as the surface-to-surface distance between the particle and the wall, as shown in the sketch of Fig. 2(a). Here the time in the plot has been scaled by the time required for a single swimmer in an unbounded fluid (with velocity $v_0 = 2/3B_1$) to move a distance equal to its radius, R/v_0. Squirmers with $\beta < 5$ are repelled from the wall, as a result of the hydrodynamic and steric interactions with the plate. The case of $\beta = 5$ is slightly different, showing a bouncing motion. To analyze the swimming orientation, we define $\delta(t) = \arccos[\hat{\boldsymbol{e}}(t) \cdot \hat{\boldsymbol{z}}]$ as the angle that the polar squirmer axis forms with the wall normal, as shown in Fig. 2(a). Figure 2(c) shows $\cos \delta(t)$ as a function of time for all the squirmer types we considered. Starting from an initial tilt angle of $\delta_0 = 135°$, all squirmers with $\beta < 5$ reach a positive final value, corresponding to an orientation that points away from the wall. In contrast, strong pullers ($\beta = 5$) exhibit a continuously varying orientation as a result of the bouncing motion over the wall. In all the cases described so far, for which $\chi = 0$, the squirmer swims in the yz plane, with no motion observed along the third x direction. The introduction of the chirality, achieved via the rotlet dipole term $\frac{3}{2}C_2 \sin 2\theta \hat{\boldsymbol{\phi}}$ in Eq. (2), does not affect the swimming height or the orientation but simply introduces a motion along the third direction x. This is shown in Fig. 3, where the trajectories of a neutral squirmer, a strong pusher ($\beta = -5$), and a strong puller ($\beta = 5$) at various chiralities are plotted in the xy plane. The black arrows indicate the direction of motion. While the neutral squirmer and the strong pusher ($\beta = -5$) eventually move in straight lines, at a seemingly random angle, the initial
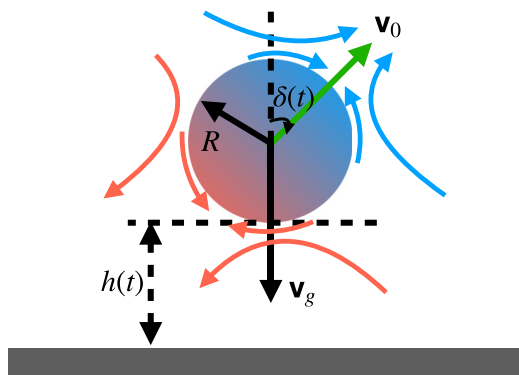
(a)
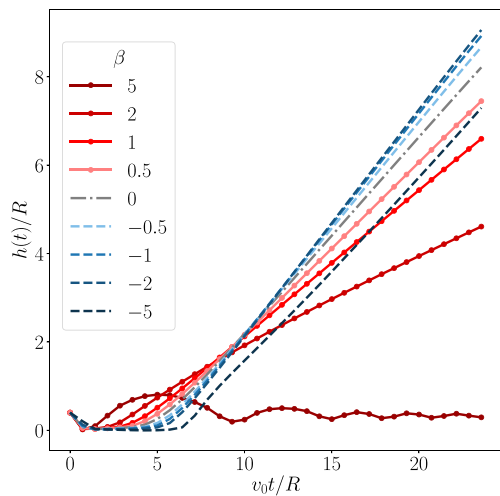
(b)
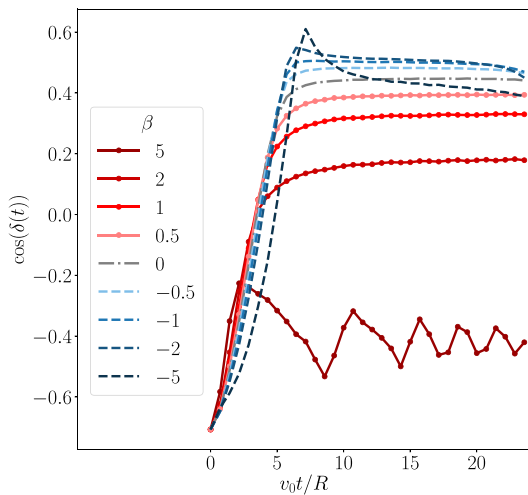
(c)

FIG. 2. (a) A schematic representation of a microswimmer (pusher with radius R) near the bottom plate. We have indicated the definitions of the height $h(t)$ and the single-particle swimming velocity v_0, oriented at an angle $\delta(t)$ from the plate normal. v_g is the sedimenting velocity when gravity is considered. (b) Swimming height and (c) orientation as a function of time for various types of squirmers with $\chi = 0$.
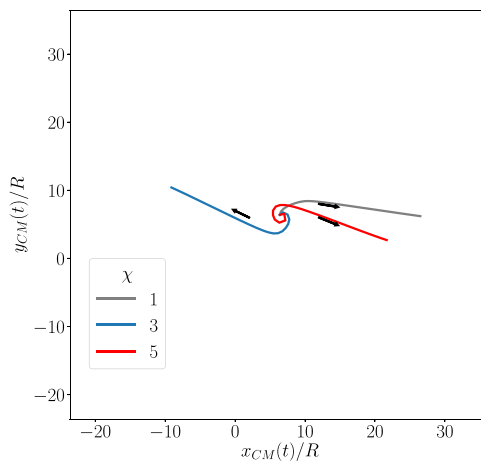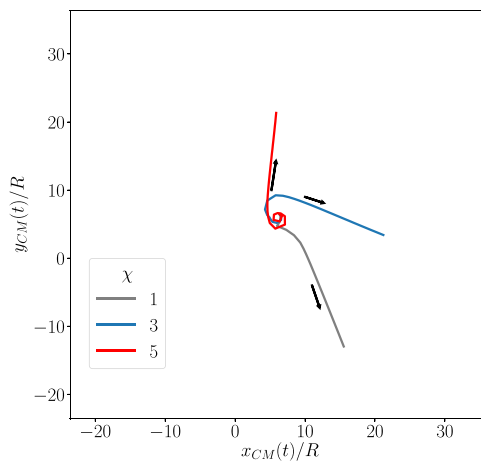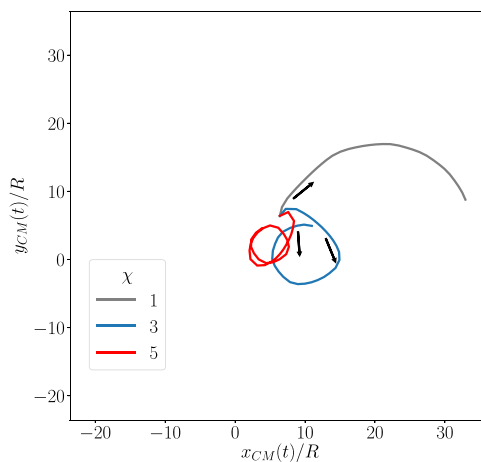
FIG. 3. Trajectories of a neutral squirmer (a), strong pusher ($\beta = -5$) (b), and strong puller ($\beta = 5$) (c) at various chiralities $\chi = 1, 3, 5$. The black arrows indicate the direction of swimming.

part of the trajectories show a clear spiral trajectory. This spiraling is stronger for larger values of χ. It is only when the neutral squirmer and the strong pusher are sufficiently far

from the plate and the interactions with the wall coming from the rotlet dipole term are negligible that the squirmer adopts a straight-line motion. This is not the case of the strong puller ($\beta = 5$), which continuously bounces on the bottom plate and, interacting with its surface, describes circular trajectories that become closer with increasing chirality (see movies S1–S3 of the Supplemental Material [56], where gravity is absent i.e., $\alpha = \infty$. Motions of a neutral squirmer (gray sphere) with $\chi = 1$, a puller-type squirmer (red sphere) with $\chi = 3$, and a pusher-type squirmer (blue sphere) with $\chi = 1$ are shown in the movies S1, S2, and S3, respectively. The arrows on the spheres represent the rotlet dipole.). We considered only the cases of positive chirality, because a negative one would simply produce reversed trajectories with respect to the positive cases.

B. Sedimentation of nonchiral swimmers

We now consider the sedimentation of a single squirmer under gravity near a solid flat wall with no chirality $\chi = 0$. It is useful to define two dimensionless parameters to characterize the dynamics. The first one is the Reynolds number, which was already mentioned above. The second dimensionless number $\alpha = v_0/v_g$ represents the strength of sedimentation, which accounts for the effect of gravity, as compared with the self-propulsion, and is defined as the ratio between the natural self-propelling velocity of the squirmer $v_0 = 2/3B_1$ and the sedimenting velocity of a corresponding passive particle $v_g = M_p g/6\pi \eta_f R$ [57–61]. If $\alpha \geqslant 1$, the self-propulsion dominates the sedimentation due to gravity; we refer to this state as a cruising regime. If $\alpha \ll 1$, the squirmer sediments to the bottom, reorients perpendicular to the plate, and finally stops due to the strong force of gravity; we refer to this state as the strong gravity regime [57]. Therefore, to observe nontrivial dynamical states, we chose $\alpha = 0.3$, which is in a moderate gravity regime, and $\alpha = 0.06$, which is in the strong gravity regime. To ensure that the squirmer sediments under gravity, a density ratio of $\rho_p/\rho_f = 5$ was used. The parameter values are the same as those of the previous section. In these simulations, we placed the squirmer in the same initial position $(L/2\Delta, L/2\Delta, L/7\Delta)$ as before, i.e., near the bottom plate, with its swimming axis aligned with the y direction and parallel to the wall. The system was then evolved until a stationary state was reached. We also performed a set of simulations starting with different initial orientations and confirmed that the squirmer always reaches the same stationary state for the range of parameter values $\beta \in [-5, 5]$ and $\chi \in [-5, 5]$ considered in the present study. Figure 4(a) shows the stationary surface to surface distance h_∞ between the squirmer and the bottom plate [see Fig. 2(a)] for various values of β in the moderate ($\alpha = 0.3$) and strong ($\alpha = 0.06$) gravity regimes. The competition between sedimentation and self-propulsion results in a nonzero separation from the bottom plate. For $\alpha = 0.06$, the gravity force is strong enough to push the squirmer down to the bottom plate, $h_\infty/R < 0.2$; this is also visible in Fig. 4(b), which shows the swimming surface-to-surface distances as functions of time for various values of β. For $\alpha = 0.3$, instead, highly asymmetric dynamics for both pushers ($\beta < 0$) and pullers

(a)

(b)

(c)
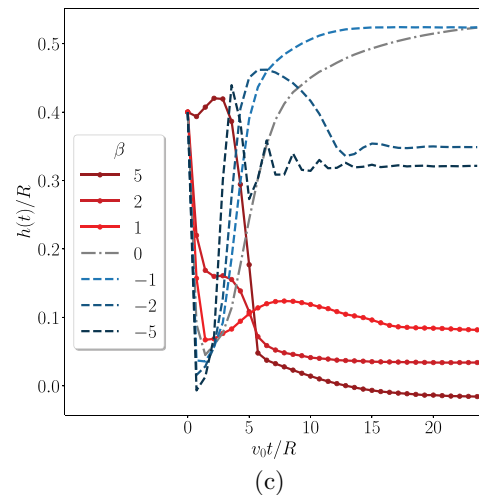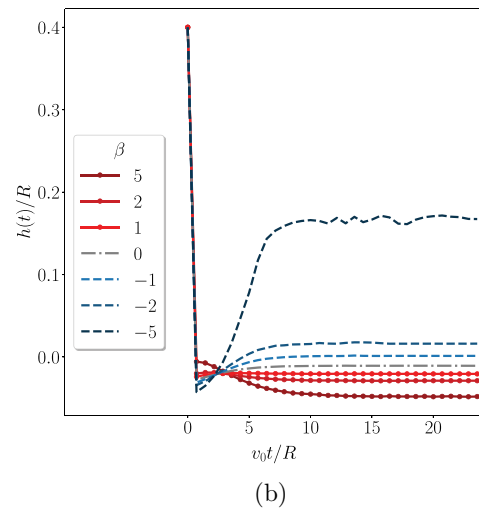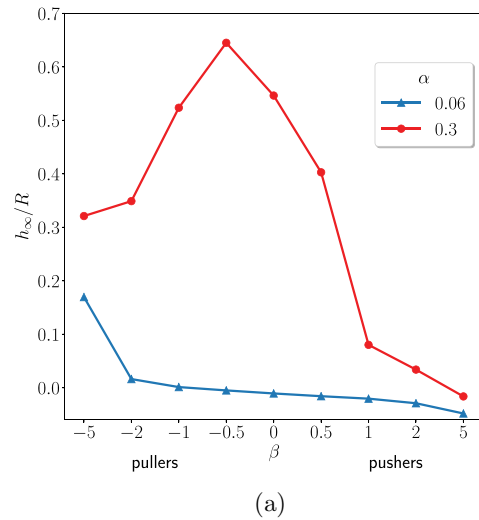
FIG. 4. (a) Stationary swimming height as a function of β for strong ($\alpha = 0.06$) and moderate ($\alpha = 0.3$) gravitational forces. Swimming heights for strong (b) and moderate (c) gravitational forces as a function of time for various values of β. Time is normalized by $\frac{R}{v_0}$, with $v_0 = 2/3B_1$ being the free swimming velocity of a squirmer in an unbounded fluid.

(a)

(b)

(c)

FIG. 5. (a) Stationary swimming orientation as a function of β for strong ($\alpha = 0.06$) and moderate ($\alpha = 0.3$) gravitational forces. Swimming heights for strong (b) and moderate (c) gravitational forces as a function of time for various values of β.

the swimming direction and the normal direction relative to the plate [as defined in Fig. 2(a)] at various values of β. In the case of strong gravity ($\alpha = 0.06$), the squirmers sediment to the bottom plate and reorient at a perpendicular direction, corresponding to $\cos(\delta_\infty) \simeq 1$, which is also visible in Fig. 5(b). In the case of moderate gravity $\alpha = 0.3$, pushers move over the wall with a tilted orientation, while neutral swimmers and pullers still reorient perpendicular to the plate, as shown in Fig. 5(c) (see movies S4–S6 of the Supplemental Material [56], where moderate gravity is applied $\alpha = 0.3$ without chirality $\chi = 0$. Motions of a neutral squirmer (gray sphere), a puller-type sqirmer (red sphere), and a pusher-type sqirmer (blue sphere) are shown in the movies S4, S5, and S6, respectively.). The fact that the pushers in Fig. 4(a) can reach stationary heights greater than those of the corresponding pullers is due to their nature of pushing fluid away along their axis of motion. In particular, the maximum stationary height for $\alpha = 0.3$ near the weak pusher condition $\beta \simeq -0.5$ is related to the stationary orientation shown in Fig. 5(a). The pushers, in contrast to the pullers, tend to develop a tilted orientation for $\beta \leqslant -0.5$. The reason for this difference can be explained as follows: when the force of gravity is very strong, for $\alpha = 0.06$, all the squirmers are very close to the bottom plate, and the induced hydrodynamic torque reorients the particle in a direction perpendicular to the plate. However, when the force of gravity is moderate, for $\alpha = 0.3$, pushers develop stable surface-to-surface distances greater than those of their puller counterparts. In this situation, the vertical direction for strong pushers ($\beta < 1$) becomes unstable, and the induced hydrodynamic torque reorients them in a tilted direction with respect to the vertical one. Under the limit of a large distance from the plate, as stated by far-field theory, the pushers should acquire a direction parallel to the plate with respect to the vertical one prescribed by near-field theory [57,59,62]. The data for $\alpha = 0.06$ from the work of Kuhr *et al.* [59] are also shown in Fig. 5(a), with the error bars indicating the magnitudes of the thermal fluctuations associated with the multiparticle collision dynamics (MPCD) used in their simulations. Excellent agreement is seen between our results and the data of Kuhr *et al.* [59] for $-2 \leqslant \beta \leqslant 2$, where the squirmers orient perpendicular to the bottom plate due to the strong gravity. However, non-negligible deviations appear for $|\beta| > 0.5$, while our results for $|\beta| < 2$ still agree with those of Kuhr *et al.*, within the error bars. We consider two possible explanations for this discrepancy: (1) Our discretization errors may be non-negligible, because we solve the governing equations on a fixed Cartesian grid with a finite spacing Δ. Although this type of error increases with increasing $|\beta|$, we confirmed that the error remains small at the present resolution $R/\Delta = 5$ in the parameter range $|\beta| \leqslant 5$ [43]. (2) The influence of thermal fluctuations cannot be excluded from the MPCD simulations used in the work of Kuhr *et al.* [59].

C. Sedimentation of chiral swimmers

We now consider the effect of adding the chirality and studying the sedimentation under gravity near a solid flat plate. For this analysis, we consider only the case of $\alpha = 0.3$. In Fig. 6 the velocity streamlines, with heat maps of the fluid velocity magnitude, around a pusher particle with $\beta = -5$ and $\chi = 0$ are shown in the (a) xy, (b) xz, and (c) yz cross sections.
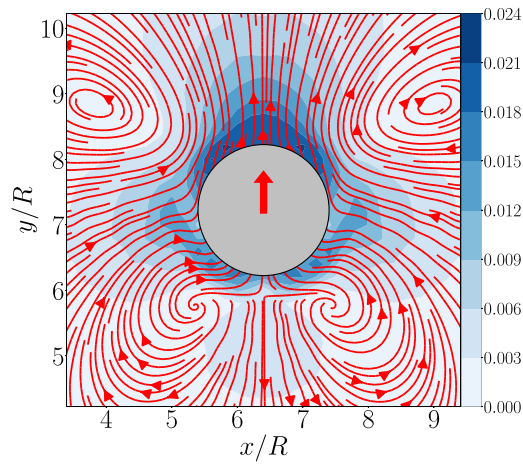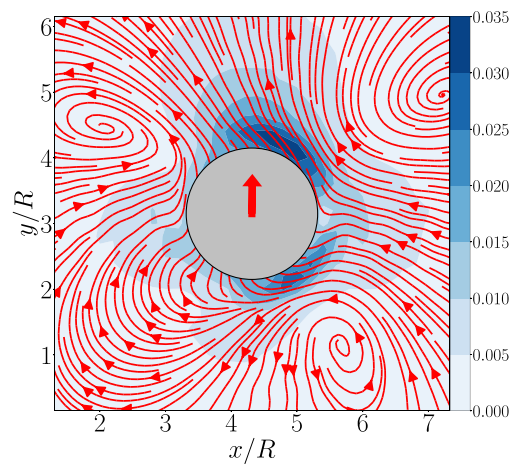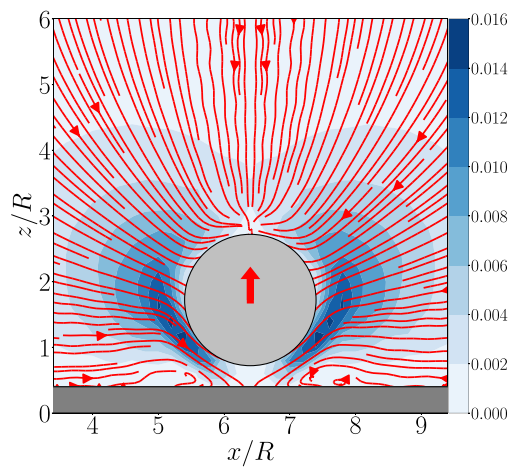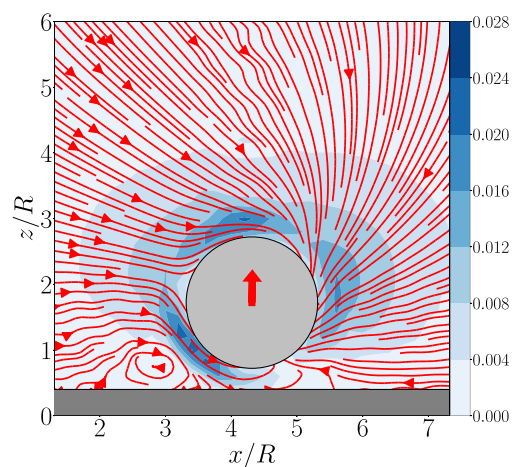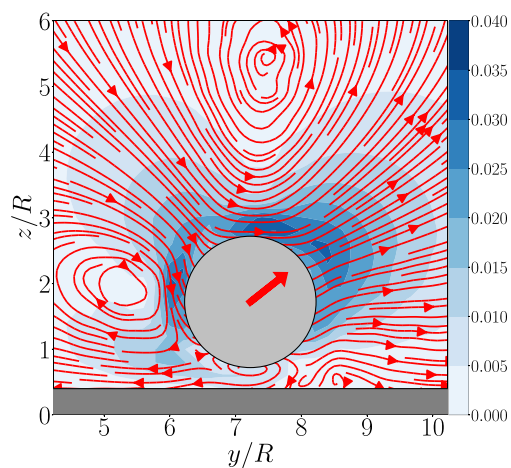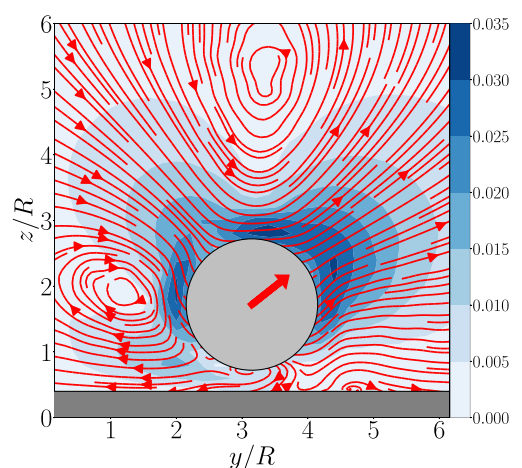
($\beta > 0$) are observed, with the stationary height being much higher than that of the strong gravity case, also shown in Fig. 4(c). Figure 5(a) shows the stationary orientations of the squirmer $\cos(\delta_\infty)$, with δ_∞ being the stable angle between

FIG. 6. The velocity streamlines, superimposed on a heat map of the magnitude of the fluid velocity, around a pusher particle with $\beta = -5$ for $\chi = 0$ and $\alpha = 0.3$ in the (a) xy, (b) xz, and (c) yz cross sections. The red internal arrows mark the swimming axis of the squirmer, and the gray rectangles indicate the position of the bottom wall.

FIG. 7. The velocity streamlines, superimposed on a heat map of the magnitude of the fluid velocity, around a pusher particle with $\beta = -5$ for $\chi = 1$ and $\alpha = 0.3$ in the (a) xy, (b) xz, and (c) yz cross sections. The red internal arrows mark the swimming axis of the squirmer, and the gray rectangles indicate the position of the bottom plate.
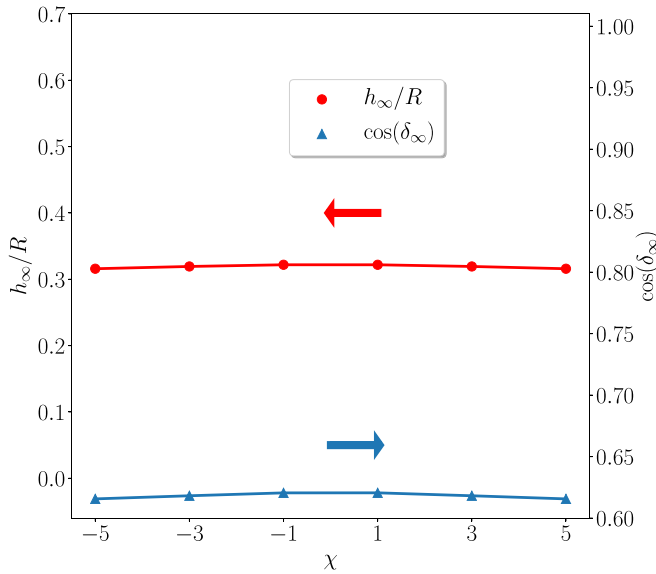
FIG. 8. The stationary height (red) and orientation (blue) of a pusher particle with $\beta = -5$ for various chiralities $-5 \leqslant \chi \leqslant 5$ under moderate gravity ($\alpha = 0.3$).

The red arrows mark the swimming axis of the squirmer, and the gray rectangle indicates the position of the wall. Figure 7 shows the same plots for a squirmer with chirality $\chi = 1$. In both Fig. 6(c) and Fig. 7(c), the characteristic pusher velocity fields are recognizable, with fluid being pushed away along the direction of the swimming axis and pulled along the perpendicular direction. A velocity vortex is clearly visible behind the particles. The differences in the velocity fields are visible in the xy and xz planes; see Fig. 6(a)(b) and Fig. 7(a)(b). In Fig. 6(a) the direction of the velocity field in front of the squirmer is aligned with the swimming axis, in contrast to its counterpart in Fig. 7(a). This is a clear sign of the fact that the trajectory of the chiral pusher in the xy plane is not a straight-line path, as was the case without chirality. In addition, the plots of Fig. 6(b) and Fig. 7(b) show clear differences, with the velocity of the latter showing a vortex structure due to the interaction of the rotlet dipole with the plate that is absent in the former.

We repeated the same analyses described in the previous section, varying the parameters β and χ and evaluating the heights and orientations of the various squirmers, and found that the introduction of chirality did not contribute to a dramatic change in these quantities. This tendency is visible in Fig. 8, where the stationary heights (left side) and orientations (right side) for the pusher $\beta = -5$ at various χ values are shown.

The physical effect of the chirality consists of a deviation in the trajectories of all the particles from a straight-line motion, observed without chirality, into a circular one. Figure 9(a) shows the trajectories of the pusher $\beta = -5$ at various chiralities. For $\chi > 0$, the squirmer performs CW circular motions; for $\chi < 0$, the trajectories become CCW. Increasing the absolute value of χ reduces the radius of the circular trajectories of the pusher (also shown in movies S7–S9 of the Supplemental Material [56], where moderate gravity is applied $\alpha = 0.3$ for a pusher-type squirmer (blue sphere)

(a)

(b)
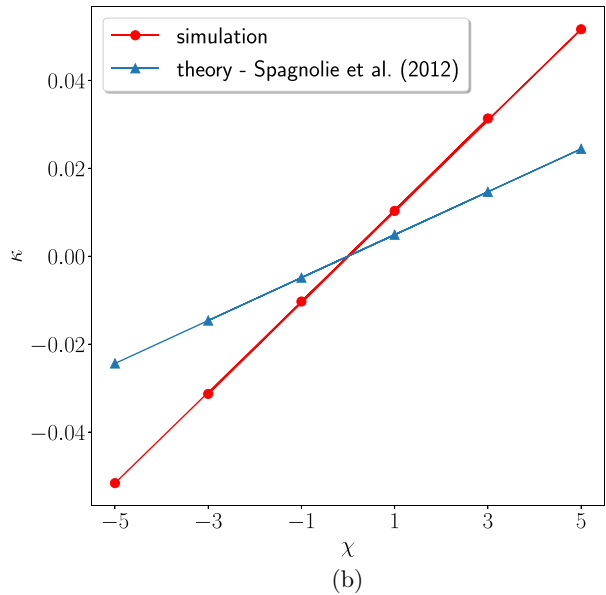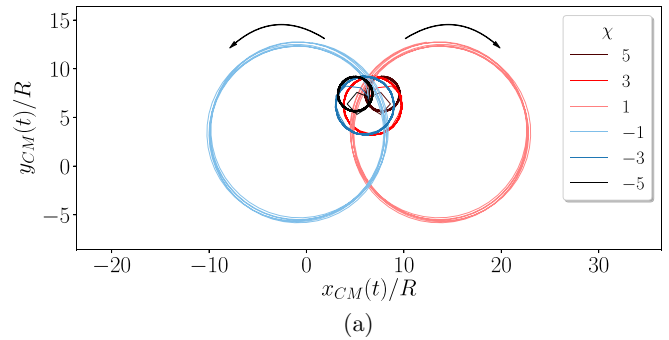
FIG. 9. (a) The trajectories of a pusher particle $\beta = -5$ at various chiralities $-5 \leqslant \chi \leqslant 5$ under moderate gravity ($\alpha = 0.3$). The black arrows indicate the CW and CCW directions of motion. (b) The curvature of the circular trajectories shown in (a) versus the chirality χ. The theoretical prediction, $\kappa = \frac{3\chi R^3}{32H^4}$, of Ref. [33] is also plotted for comparison.

with chirality $\chi = 1$, 3, and 5 in the movies S7, S8, and S9, respectively). We evaluated the radius of curvature according to [63]

$$R_c = \frac{(\dot{x}_{CM}^2 + \dot{y}_{CM}^2)^{3/2}}{\dot{x}_{CM}\ddot{y}_{CM} - \dot{y}_{CM}\ddot{x}_{CM}}, \qquad (12)$$

where the dots denote the temporal derivative and the curvature is defined as $\kappa = R_c^{-1}$. If $\chi = 0$, the squirmer trajectory is always straight; thus, $\kappa = 0$.

Figure 9(b) shows the curvature κ of the pusher $\beta = -5$ at various chiralities χ, together with the theoretical prediction, $\kappa = \frac{3\chi R^3}{32H^4}$, proposed by Spagnolie $et\ al.$ [33], Lopez $et\ al.$ [34], and Papavassiliou $et\ al.$ [64,65].

The simulated curve is obtained by fixing the height of the squirmer and keeping its orientation parallel to the bottom plate, as assumed in Refs. [33,34,64,65]. Both curves show a linear trend, which suggests an increase in the curvature upon increasing the magnitude of the chirality. However, we note that a systematic difference appears, with our simulation results predicting larger values of $|\kappa|$ for $\chi \neq 0$. We believe

that this is due to the far-field approximation that was used in Refs. [33,34,64,65] to derive the theoretical expression. This approximation has been demonstrated to be valid for spherical swimmers, but it assumes that the distance between the swimmer and the surface of the wall is much larger than its diameter. At shorter distances, such as those seen in our simulations, we expect this approximation to yield less accurate results.

IV. DISCUSSION

Various works considered squirmers near surfaces [62,66–68] and included sedimentation [55,57–61]; however, the role of chirality has not been considered in detail. In the present study, we have attempted to fill this gap by studying the dynamics of both sedimenting and nonsedimenting squirmers with and without chirality under similar conditions.

With regard to swimming in the absence of sedimentation, the results for $\chi = 0$ are consistent with previous studies that observed a repulsive behavior for neutral swimmers and pushers and bouncing dynamics for pullers [62,66–68]. In the case of sedimenting squirmers, Shen *et al.* found that neutral swimmers and weak pullers and pushers reorient in the direction perpendicular to the bottom wall [60], consistent with our simulation results, as shown in Fig. 5(a). The stationary heights for pushers is higher than that for pullers and neutral swimmers because the fluid flows behind pushers are stronger. These results are also consistent with the MPCD simulations of Rühle *et al.* [57], who considered the dynamics of a single squirmer under gravity but without chirality for various values of α and β. As previously reported, the introduction of chirality affects the trajectories of the swimmers, which transition from a straight-line motion, in the absence of chirality, to curved trajectories, in the presence of gravity. The curved trajectories and the resulting curvature values for $\beta = -5$ and various χ, as shown in Fig. 9(a) and 9(b), are consistent with previously reported results. In Fig. 9(a) the trajectories for a strong pusher ($\beta = -5$) with different values of χ are shown. In the case of $\chi > 0$ ($\chi < 0$), the pusher exhibits CW (CCW) trajectories. This result is consistent with the previous work of Ishimoto *et al.* [68], who limited the analysis to the case of a neutral squirmer, as well as that of Elgeti *et al.*, who studied the dynamics of sperm near surfaces [69]. The CW circular trajectories of *E. coli* have also been experimentally observed near a rigid boundary [7–11]. We are aware that *E. coli* is an elongated bacterium equipped with flagella that allow it to move. The spherical chiral squirmer model adopted in this work represents a strong approximation, as real microswimmers are not necessarily spherical. Although the spheroidal shape can be introduced in the model [68], it still neglects the detailed propulsion mechanics, replacing them with a prescribed surface velocity field. However, despite its simplicity, we still think that the spherical chiral squirmer model is a useful tool for modeling real microorganisms, as it is capable of reproducing, at least on a qualitative or semiquantitative level, experimental results similar to the circular trajectories of *E. coli* [7–11]. A recent theoretical and numerical study by Park *et al.* on flagellated bacteria near walls presented a

more accurate model, in which the bacterium was modeled with a spheroidal cell body with a single oscillating flagellum [70]. They recovered the circular trajectories near the wall and showed how varying the aspect ratio of the cell body modifies the radius of curvature. Ishimoto *et al.* [68] previously considered a chiral spheroidal squirmer near a plate but only for the case of a neutral swimmer $\beta = 0$ without the effect of gravity. Here we performed a systematic study including pushers and pullers but focused only on spherical swimmers. We studied the dynamics of a squirmer near a flat plate, initially neglecting the effect of gravity, and then extended the analysis to consider the role of sedimentation. *E. coli* has been mentioned as a typical microorganism with which to compare our results. Although its does not, as far as we know, sediment, it is often referenced as a typical chiral organism. In the presence of gravity, which is known to cause real swimmers to exhibit rich dynamical behavior, such as the waltz and minuet motion of *Volvox* algae [21] and the sedimentation of phytoplankton [28], we expect chiral squirmers to show similarly rich dynamical modes. Finally, it is shown in Fig. 9(b) that the linear dependency of the curvature on the chirality $\kappa \propto \chi$ is in semiquantitative agreement with the far-field theoretical predictions [33].

V. SUMMARY

In this work, we have studied the dynamics of a single squirmer near a flat plate in the presence and absence of sedimentation by taking into account the chirality through the rotlet dipole term in the surface velocity. When gravity and chirality are neglected and the squirmer swims near the plate, the previous results of the literature are recovered [62,66–68]. The introduction of chirality simply adds motion in the third direction of the system. In the case of sedimentation, different dynamics emerge upon varying the gravity strength. In the absence of chirality, for strong gravity, all types of squirmers sediment to the bottom plate and reorient in the perpendicular direction. In contrast, for moderate gravity, pushers tend to tilt from the perpendicular direction and continuously swim in this tilted direction over the bottom plate. While the introduction of chirality does not alter the stationary height and orientation of the squirmer significantly, it does distort its trajectories, which show an increasing curvature upon increasing the magnitude of the chirality. The present study on chiral swimmers will be extended to consider the collective behaviors of sedimenting squirmer suspensions [55,58–61]. Combinatory applications of gravity, confinement, chirality, and swimming type and strength are expected to lead to the appearance of rich dynamical states requiring investigation.

[1] E. Lauga and T. R. Powers, Rep. Prog. Phys. **72**, 096601 (2009).

[2] M. C. Marchetti, J. F. Joanny, S. Ramaswamy, T. B. Liverpool, J. Prost, M. Rao, and R. A. Simha, Rev. Mod. Phys. **85**, 1143 (2013).

[3] J. Elgeti, R. G. Winkler, and G. Gompper, Rep. Prog. Phys. **78**, 056601 (2015).

[4] C. Bechinger, R. Di Leonardo, H. Löwen, C. Reichhardt, G. Volpe, and G. Volpe, Rev. Mod. Phys. **88**, 045006 (2016).

[5] A. Zöttl and H. Stark, J. Phys.: Condens. Matter **28**, 253001 (2016).

[6] M. R. Shaebani, A.Wysocki, R. G. Winkler, G. Gompper, and H. Rieger, Nat. Rev. Phys. **2**, 181 (2020).

[7] W. R. DiLuzio, L. Turner, M. Mayer, P. Garstecki, D. B. Weibel, H. C. Berg, and G. M. Whitesides, Nature (London) **435**, 1271 (2005).

[8] E. Lauga, W. DiLuzio, G. M. Whitesides, and H. A. Stone, Biophys. J. **90**, 400 (2006).

[9] R. Di Leonardo, D. Dell'Arciprete, L. Angelani, and V. Iebba, Phys. Rev. Lett. **106**, 038101 (2011).

[10] S. Bianchi, F. Saglimbeni, G. Frangipane, D. Dell'Arciprete, and R. Di Leonardo, Soft Matter **15**, 3397 (2019).

[11] S. Bianchi, F. Saglimbeni, and R. Di Leonardo, Phys. Rev. X **7**, 011010 (2017).

[12] J. Hu, M. Yang, G. Gompper, and R. G. Winkler, Soft Matter **11**, 7867 (2015).

[13] T. Yamamoto and M. Sano, Soft Matter **13**, 3328 (2017).

[14] T. Yamamoto and M. Sano, Phys. Rev. E **97**, 012607 (2018).

[15] T. Yamamoto and M. Sano, Phys. Rev. E **99**, 022704 (2019).

[16] E. Tjhung, M. E. Cates, and D. Marenduzzo, Proc. Natl. Acad. Sci. USA **114**, 4631 (2017).

[17] L. N. Carenza, G. Gonnella, D. Marenduzzo, and G. Negro, Proc. Natl. Acad. Sci. USA **116** (44), 22065 (2019).

[18] H. Löwen, Eur. Phys. J.: Spec. Top. **225**, 2319 (2016).

[19] F. Kümmel, B. ten Hagen, R. Wittkowski, I. Buttinoni, R. Eichhorn, G. Volpe, H. Löwen, and C. Bechinger, Phys. Rev. Lett. **110**, 198302 (2013).

[20] D. Das and E. Lauga, Phys. Rev. E **100**, 043117 (2019).

[21] K. Drescher, K. C. Leptos, I. Tuval, T. Ishikawa, T. J. Pedley, and R. E. Goldstein, Phys. Rev. Lett. **102**, 168101 (2009).

[22] V. Kantsler, J. Dunkel, M. Polin, and R. E. Goldstein, Proc. Natl. Acad. Sci. USA **110**, 1187 (2013).

[23] M. Enculescu and H. Stark, Phys. Rev. Lett. **107**, 058301 (2011).

[24] B. ten Hagen, F. Kümmel, R. Wittkowski, D. Takagi, H. Löwen, and C. Bechinger, Nat. Commun. **5**, 4829 (2014).

[25] K. Wolff, A. M. Hahn, and H. Stark, Eur. Phys. J. E **36**, 43 (2013).

[26] C. Krüger, C. Bahr, S. Herminghaus, and C. Maass, Eur. Phys. J. E **39**, 64 (2016).

[27] W. M. Durham, J. O. Kessler, and R. Stocker, Science **323**, 1067 (2009).

[28] A. Sengupta, F. Carrara, and R. Stocker, Nature (London) **543**, 555 (2017).

[29] M. J. Lighthill, Commun. Pure Appl. Math. **5**, 109 (1952).

[30] J. R. Blake, J. Fluid Mech. **46**, 199 (1971).

[31] E. Lauga, Annu. Rev. Fluid Mech. **48**, 105 (2016).

[32] A. Poddar, A. Bandopadhyay, and S. Chakraborty, J. Fluid Mech. **894**, A11 (2020).

[33] S. E. Spagnolie and E. Lauga, J. Fluid Mech. **700**, 105 (2012).

[34] D. Lopez and E. Lauga, Phys. Fluids **26**, 071902 (2014).

[35] S. Kim and S. J. Karrila, *Microhydrodynamics: Principles and Selected Applications* (Butterworth-Heinemann, Oxford, 1991).

[36] O. Pak and E. Lauga, J. Eng. Math. **88**, 1 (2014).

[37] T. J. Pedley, D. R. Brumley, and R. E. Goldstein, J. Fluid Mech. **798**, 165 (2016).

[38] N. Oyama, J. J. Molina, and R. Yamamoto, Phys. Rev. E **93**, 043114 (2016).

[39] N. Oyama, J. J. Molina, and R. Yamamoto, Eur. Phys. J. E **40**, 95 (2017).

[40] N. Oyama, J. J. Molina, and R. Yamamoto, arXiv:1612.00135.

[41] Y. Nakayama and R. Yamamoto, Phys. Rev. E **71**, 036707 (2005).

[42] Y. Nakayama, K. Kim, and R. Yamamoto, Eur. Phys. J. E **26**, 361 (2008).

[43] J. J. Molina, Y. Nakayama, and R. Yamamoto, Soft Matter **9**, 4923 (2013).

[44] A. Hamid and R. Yamamoto, J. Phys. Soc. Jpn. **82**, 024004 (2013).

[45] N. Shakeel, A. Hamid, A. Ullah, J. J. Molina, and R. Yamamoto, J. Phys. Soc. Jpn. **87**, 064402 (2018).

[46] A. Hamid and R. Yamamoto, Phys. Rev. E **87**, 022310 (2013).

[47] A. Hamid, J. J. Molina, and R. Yamamoto, RSC Adv. **4**, 53681 (2014).

[48] A. Hamid, J. J. Molina, and R. Yamamoto, Soft Matter **9**, 10056 (2013).

[49] T. Ishikawa, M. P. Simmonds, and T. J. Pedley, J. Fluid Mech. **568**, 119 (2006).

[50] T. Ishikawa and T. J. Pedley, J. Fluid Mech. **588**, 399 (2007).

[51] T. Ishikawa and T. J. Pedley, J. Fluid Mech. **588**, 437 (2007).

[52] T. Ishikawa, J. T. Locsei, and T. J. Pedley, J. Fluid Mech. **615**, 401 (2008).

[53] T. Ishikawa and T. J. Pedley, Phys. Rev. Lett. **100**, 088103 (2008).

[54] T. Ishikawa, J. Fluid Mech. **705**, 98 (2012).

[55] F. Rühle and H. Stark, arXiv:2002.04323v1.

[56] See Supplemental Material at http://link.aps.org/supplemental/10.1103/PhysRevE.101.052608 for the movies.

[57] F. Rühle, J. Blaschke, J.-T. Kuhr, and H. Stark, New J. Phys. **20**, 025003 (2018).

[58] J.-T. Kuhr, J. Blaschke, F. Rühle, and H. Stark, Soft Matter **13**, 7548 (2017).

[59] J.-T. Kuhr, F. Rühle, and H. Stark, Soft Matter **15**, 5685 (2019).

[60] Z. Shen and J. S. Lintuvuori, Phys. Rev. Fluids **4**, 123101 (2019).

[61] Z. Shen, A. Würger, and J. S. Lintuvuori, Soft Matter **15**, 1508 (2019).

[62] J. S. Lintuvuori, A. T. Brown, K. Stratford, and D. Marenduzzo, Soft Matter **12**, 7959 (2016).

[63] L. Dorst, D. Fontijne, and S. Mann, *Geometric Algebra for Computer Science: An Object Oriented Approach to Geometry* (Morgan Kaufmann Publishers, Burlington, MA, 2007).

[64] D. Papavassiliou and G. P. Alexander, Europhys. Lett. **110**, 44001 (2015).

[65] D. Papavassiliou and G. P. Alexander, J. Fluid Mech. **813**, 618 (2017).

[66] Z. Shen, A. Würger, and J. S. Lintuvuori, Eur. Phys. J. E **41**, 39 (2018).

[67] G.-J. Li and A. M. Ardekhani, Phys. Rev. E **90**, 013010 (2014).

[68] K. Ishimoto and E. A. Gaffney, Phys. Rev. E **88**, 062702 (2013).

[69] J. Elgeti, U. Kaupp, and G. Gompper, Biophys. J. **99**, 1018 (2010).

[70] Y. Park, Y. Kim, and S. Lim, Phys. Rev. E **100**, 063112 (2019).